Minimizing energy storage utilization in a stand-alone dc microgrid using photovoltaic flexible power control

Yan, Hein Wai; Narang, Aditi; Tafti, Hossein Dehghani; Farivar, Glen G.; Ceballos, Salvador; Pou, Josep

2021

Yan, H. W., Narang, A., Tafti, H. D., Farivar, G. G., Ceballos, S. & Pou, J. (2021). Minimizing energy storage utilization in a stand-alone dc microgrid using photovoltaic flexible power control. IEEE Transactions On Smart Grid, 12(5), 3755-3764. https://dx.doi.org/10.1109/TSG.2021.3073370

https://hdl.handle.net/10356/150189

https://doi.org/10.1109/TSG.2021.3073370

Minimizing Energy Storage Utilization in a Stand-Alone DC Microgrid Using Photovoltaic Flexible Power Control

Hein Wai Yan, *Student Member, IEEE,* Aditi Narang, *Student Member, IEEE,*
Hossein Dehghani Tafti, *Senior Member, IEEE*, Glen G. Farivar, *Senior Member, IEEE*,
Salvador Ceballos, Josep Pou*, Fellow, IEEE*

***Abstract*—DC microgrids (dcMGs) are gaining popularity for photovoltaic (PV) applications as the demand for PV generation continues to grow exponentially. A hybrid control strategy for a PV and battery energy storage system (BESS) in a stand-alone dcMG is proposed in this paper. In contrast to the conventional control strategies that regulate the dc-link voltage only with the BESS, the proposed control strategy exploits both the PV system and the BESS to regulate the dc-link voltage. The PV acts as the primary dc voltage regulator allowing for the battery to remain standby as a secondary dc voltage regulating resource. As a result, the proposed control strategy minimizes the utilization of the BESS in order to prolong its lifetime while maintaining the state-of-charge (SoC) of the battery within a desired range. To achieve that, the flexible power point tracking (FPPT) concept is applied to the PV system to enhance the dynamic performance of the dcMG by adaptively adjusting the PV output power according to the load profile. The performance of the proposed control strategy is verified with experimental results. Furthermore, the effectiveness of the proposed control strategy on prolonging the lifetime of a lithium-ion battery and a lead-acid battery is investigated via a simulation case study with one-day load and irradiance curve profiles.**

***Index Terms*—Battery energy storage system (BESS), battery state-of-charge (SoC), dc microgrid (dcMG), flexible power point tracking (FPPT), photovoltaic (PV).**

I. Introduction

Renewable energy resources are rapidly replacing conventional fuels to generate electricity in order to achieve energy sustainability, and reduce the carbon footprint [1]. Solar energy is one of the most abundantly available renewable resources and hence, photovoltaic (PV) power generation share is steadily increasing.

DC microgrid (dcMG) power systems are drawing great attention due to the steady growth in dc load demand and renewable dc sources. The majority of modern consumer electronics such as energy-efficient lighting systems and energy-saving electronics are operated with dc supply. Furthermore, PV modules and batteries are intrinsically dc components. Therefore, by using a dcMG to transfer power from dc sources to dc loads would eliminate the necessity of having dc-to-ac conversion stages on the generation side and ac-to-dc conversion stages on the load side. Also, synchronization and reactive power flow issues are null in dcMGs [2], [3]. Such dc systems are used in a broad range of applications including ships, automobiles, telecommunication stations, etc. However, issues associated with dynamically changing weather conditions and dc-link voltage transients may lead to instability in the microgrid and hence, dcMGs require a robust control scheme.

The majority of existing PV controllers aim to extract the maximum power from the PV arrays using maximum power point tracking (MPPT) algorithms [4], [5], and the battery energy storage system (BESS) deals with the power difference between the load and the PV generation. Nowadays, with falling PV energy cost, supersizing the PV capacity just for the purpose of having more PV energy during the afternoon hours is a common practice and makes perfect economic sense in many cases [6]–[9]. As the PV capacity increases, its effect on grid parameters will increase as well. Therefore, the PV system should play a bigger role by participating in grid stabilization. When the PV capacity increases, MPPT operation may cause dc-link over-voltage and the BESS overcharging issues. Hence, the MPPT method alone is insufficient to control the PV generation and additional features are needed to help maintain the dc-link voltage [6].

The excessive PV penetration issue is solved with MPPT-droop dual-mode control strategy with the BESS [10]–[13]. However, the controller for the PV generation in [10] generates disturbances on the dc-link voltage during operation mode transitions and the transition criteria itself complicates the control algorithm. The PV controller in [11] only focuses on the dc-link voltage regulation, and the algorithm in [12] only focuses on the MPPT operation mode. Therefore, an additional outer-loop controller is required to extract the maximum power from the PV in [11], and to regulate the dc-link voltage in [12]. An MPPT and droop-integrated control method is introduced in [13] to eliminate the system disturbances by avoiding the control reconfiguration during operation mode transitions. The droop controller regulator is the key element in the control that provides a duty ratio for the dc-dc converter by calculating the required change of the power with the droop coefficient. However, the PV controllers in [10]–[13] operate with the constant voltage-step to adjust the PV generation, resulting a slow dynamic response under rapid environmental changes. Hence, the battery is the primary dc-link voltage controller and operates continuously (charge/discharge) to effectively regulate the dc voltage fluctuations, which are mainly imposed by the load demand transients and the intermittent irradiance

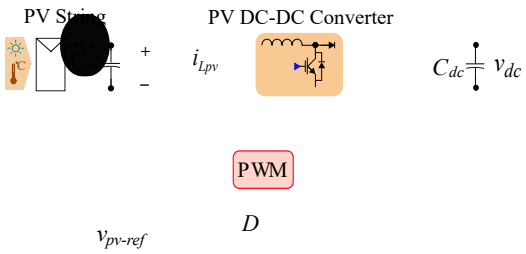
PV String
PV DC-DC Converter
+
–
i_{Lpv}
C_{dc}
v_{dc}
PWM
D
$v_{pv\text{-}ref}$

of these control limits denoted by $\triangle V$. These deadbands are set to prevent the battery from turning on and off recursively around the boundary limits. The PV maximum power $p_{pv\text{-}max}$ is estimated using the approach in [9]. Op represents the battery operation mode ($Op=-1$ shows charge mode, $Op=0$ shows standby mode and $Op=1$ shows discharge mode) and p_{load} is the load power. Subsequently, the battery SoC level is estimated using (1).

$$SoC(k) = SoC(k-1) - \int_{(k-1)T_s}^{kT_s} (i_{bat}/C_{bat})\, dt, \qquad (1)$$

where k is the sample number, T_s is the time-step, i_{bat} is the battery current, and C_{bat} is the battery capacity. If the battery current is negative (current is flowing towards the battery), the SoC will increase and vice versa, the SoC will decrease if i_{bat} is positive (battery is discharging). The rate of SoC change is directly proportional to i_{bat}.

As shown in Fig. 3, if p_{load} is larger than the maximum available power $p_{pv\text{-}max}$, ($p_{load} > p_{pv\text{-}max}$), the BESS will operate and discharge the stored energy ($Op = 1$, discharge mode) as the load demand is higher than the maximum power supply from the PV. Otherwise, Op will be updated accordingly based on the dc-link voltage v_{dc} fluctuation. For instance, if v_{dc} is greater than $V_{dc\text{-}u} + \triangle V$, the battery regulates the dc-link voltage by absorbing the power from the dc bus ($Op=-1$, charge mode). Similarly, if v_{dc} is smaller than $V_{dc\text{-}l} - \triangle V$, shown in Fig. 3, the battery discharges as v_{dc} deviation is out of the allowed band and thereby, v_{dc} is regulated by the BESS to the innermost boundaries, $V_{dc\text{-}u} - \triangle V$ and $V_{dc\text{-}l} + \triangle V$. This function is added to the controller to ensure the stability of the dcMG under sudden large step changes of the load, during which the PV converter may not provide the required fast transient response.

Once the battery is able to regulate the dc-link voltage v_{dc} into the innermost boundaries, the battery SoC is compared with its reference value SoC_{th}. If the SoC is lower than SoC_{th}, Op is updated to -1 and the battery is put into operation (charge mode) to be charged by the PV excess power generation ($p_{pv\text{-}max} - p_{load}$). Once the battery SoC reaches to SoC_{max}, the battery controller is switched off ($Op = 0$, standby mode) and only the PV converter controller is responsible for converging v_{dc} to its reference value $V_{dc\text{-}ref}$. Such threshold range (where the battery does not need to charge), as shown in Fig. 3, is implemented to reduce the micro-cycle operations when the load transients occur frequently. If v_{dc} is within the deadband zones, Op value will not be updated. When determining SoC_{th} value, there are numerous factors that need to be considered (i.e. types of battery and their chemical characteristics, charge/discharge rate, working temperature, SoC level and the load profile). Higher SoC_{th} value will increase the number of micro-cycles while the lower value risks having lower stored energy. With the proposed control methodology, the BESS utilization and the number of partial charge/discharge cycles is substantially reduced. As a result, the battery lifetime is prolonged.

According to the above discussions and the flowchart in Fig. 3, the following conditions need to be satisfied in order to keep the battery in the standby mode: (i) the battery SoC is higher than SoC_{th} (which translates that the battery does not need to charge), (ii) PV system has sufficient power for the load demand ($p_{pv\text{-}max} > p_{load}$), and (iii) v_{dc} fluctuation is within the pre-defined voltage limits (PV is able to regulate v_{dc} to its reference value $v_{dc\text{-}ref}$).

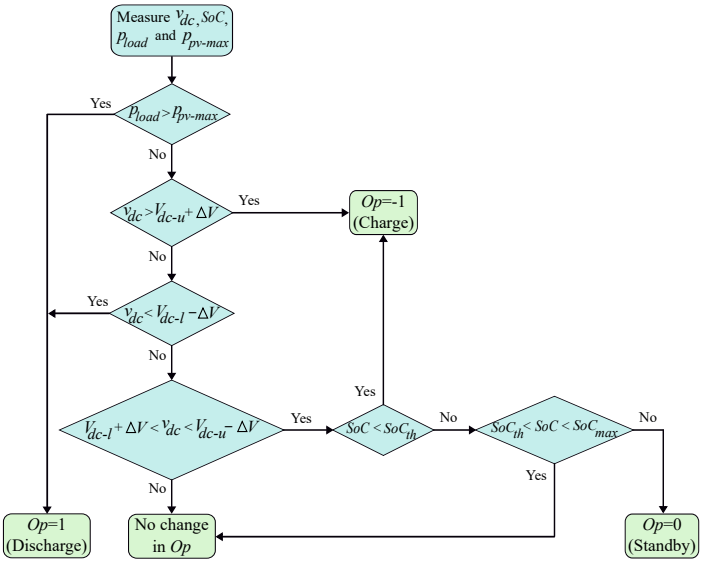

Fig. 3. Proposed hybrid operation mode identification strategy.

The PV power reference $p_{pv\text{-}ref}$ is given by:

$$p_{pv\text{-}ref} = \begin{cases} p_{load} + dp & , Op = 0 \\ p_{pv\text{-}max} & , Op \neq 0 \end{cases} \qquad (2)$$

The PV controller collects the Op, $p_{pv\text{-}max}$ and p_{load} information to determine $p_{pv\text{-}ref}$. If Op is not 0, the battery is in operation and thus, $p_{pv\text{-}ref}$ is set to $p_{pv\text{-}max}$. Hence, the PV operates at its maximum power point in order to either reduce the load share of the BESS as much as possible (when $p_{load} > p_{pv\text{-}max}$), or to restore the battery SoC to SoC_{max} (when the battery needs to restore energy). If Op is 0, it translates that the battery is not in operation. Thus, the PV will completely take control of v_{dc} regulation by adjusting $p_{pv\text{-}ref} = p_{load} + dp$. The variable dp is the output of a proportional integral (PI) controller which regulates the dc-link voltage v_{dc} to its reference value $V_{dc\text{-}ref}$, as depicted in Fig. 1.

B. PV Connected DC-DC Converter Controller

As shown in Fig. 1, the amount of power supply from the PV is controlled by a dc-dc boost converter. A FPPT algorithm is used to track $p_{pv\text{-}ref}$ in the proposed hybrid control strategy. The FPPT algorithm calculates the PV voltage reference $v_{pv\text{-}ref}$, which is then given to a model-based analytical voltage controller that generates the PV converter's inductor

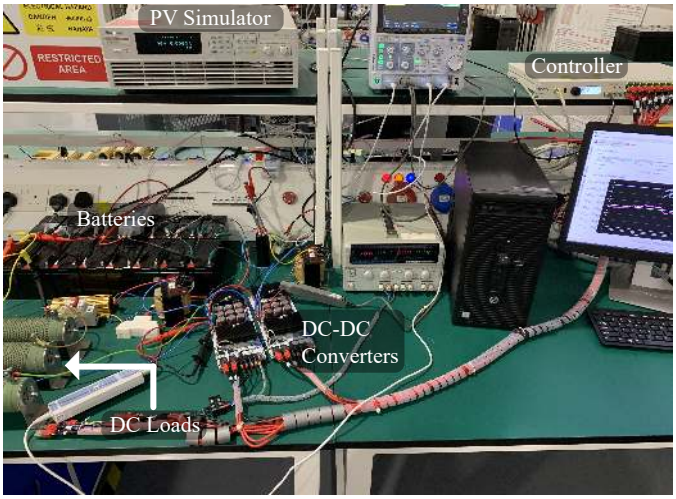

Fig. 4. Experimental setup of the standalone hybrid dcMG with BESS and PV system.

current reference, $i_{Lpv\text{-}ref}$ [20]. An indirect model predictive current controller is applied to determine the duty cycle D of the dc-dc boost converter. The PV voltage and current controllers are explained in details in [20]. The switching signals of the boost converter are generated with pulse-width modulation (PWM) technique. The main advantage of this control scheme is its fast transient response, which enables the PV system to quickly adjust the PV power based on the load demand.

C. ESS Connected DC-DC Converter Controller

A bi-directional buck/boost dc-dc converter is employed to charge/discharge the battery. The battery controller has two layers. At the outer voltage control layer, the dc-link voltage v_{dc} is regulated to $V_{dc\text{-}ref}$ by utilizing a PI controller that generates the battery inductor current reference, $\triangle i_{ess\text{-}out}$. At the inner current control layer, a model predictive current controller is implemented to ensure that this current reference is closely followed by the inductor current. The switching signals for the converter are determined by using a direct model predictive control methodology, which targets minimizing the following objective function J. Minimum value of J indicates that the inductor current closely follows its reference value.

$$J(k) = (i_{Lbat\text{-}ref}(k) - i_{Lbat}(k+1))^2, \tag{3}$$

in which,

$$i_{Lbat}(k+1) = (v_{Lbat}(k) \times T_{step})/L + i_{Lbat}(k), \tag{4}$$

$$i_{Lbat\text{-}ref}(k) = i_{ess\text{-}out\text{-}ref}(k) \times v_{dc}(k)/v_{bat}(k), \tag{5}$$

where $i_{Lbat}(k)$ represents the BESS converter's inductor current, $i_{Lbat}(k+1)$ is the predicted current at the next time-step $(k+1)$, $v_{Lbat}(k)$ is the voltage across the inductor, T_{step} is the sampling time-step, $i_{ess\text{-}out\text{-}ref}(k)$ represents the BESS output current reference determined by a PI controller and the feedforward $i_{ess\text{-}out\text{-}ff}(k)$, which equates $(p_{load} - p_{pv})/v_{dc}$ as shown in Fig. 1. In this converter, $S1$ and $S2$ are complementary and hence, there are two switching states. When $S2 = 1$, then $v_{Lbat} = v_{bat}$, and when $S1 = 1$, then $v_{Lbat} = v_{bat} - v_{dc}$. At each sampling instant, the state that produces less error (minimizes the objective function J) is chosen and the respective switching signals are provided to the BESS converter.

TABLE I
EXPERIMENTAL PARAMETERS

Parameters	Values
DC-link voltage reference, $V_{dc\text{-}ref}$	180 V
DC-link voltage upper limit, $V_{dc\text{-}u}$	188 V
DC-link voltage lower limit, $V_{dc\text{-}l}$	172 V
Voltage at maximum power point, V_{mpp}	110 V
PV maximum power, $P_{pv\text{-}max}$	800 W
Battery voltage rating, V_{bat}	96 V
Battery capacity, E_{bat}	1200 Wh
Battery dc-dc converter inductance, L_{bat}	2 mH
PV dc-dc converter inductance, L_{pv}	2 mH
PV-side capacitor, C_{pv}	0.33 mF

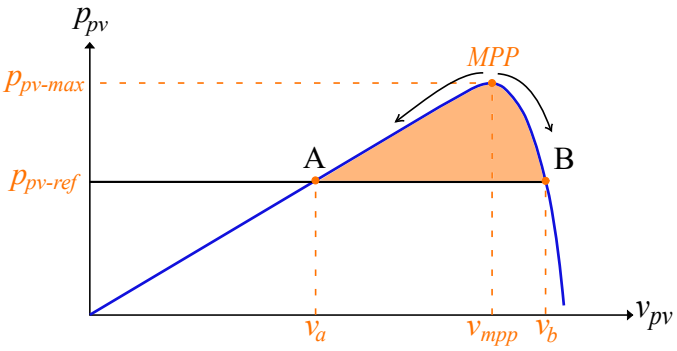

Fig. 5. Illustration of the PV operation region on the P-V curve.

III. EXPERIMENTAL RESULTS

The performance of the proposed control strategy is verified experimentally under intermittent irradiance changes and different loading conditions with a hardware setup shown in Fig. 4. The parameters of the experimental setup are provided in Table. I. The results in this section are based on the assumption of having a constant PV cell temperature of 25 °C. As shown in Fig. 5, there are two possible operating points for the PV power reference $p_{pv\text{-}ref}$: Point A on the left-side of the maximum power point (MPP) and point B on the right-side of the MPP [7], [8]. Operating at the right-side of the MPP provides a faster dynamic response than operating at the left side as a small PV voltage change results in a large power deviation. However, the disadvantage is that the PV output power will have a higher oscillation even at the steady-state condition. If the PV operates at the left-side of the MPP, the PV output power benefits from lower power oscillation at the

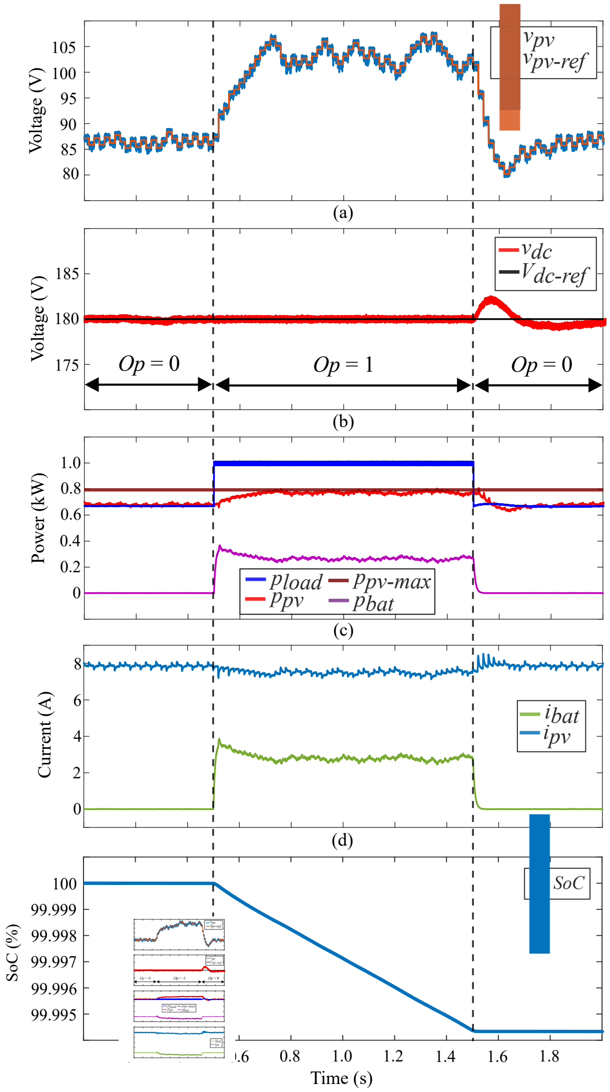

Fig. 6. *Case I*: Experimental verification of the transient response of the proposed control strategy under different loading conditions. (a) PV voltage, (b) dc-link voltage, (c) PV power, PV maximum power, load power and battery power, (d) PV and battery currents, and (e) SoC.

cost of slower dynamic performance as compared to the right-side of MPP operation. In the experimentation, the controller limits the PV operation to the left-side of the MPP to attain the low power oscillation while the dynamic is enhanced by utilizing variable voltage-step.

Case I: In this case study, the performance of the proposed control strategy under different loading conditions is examined and results are shown in Fig. 6. The SoC threshold limit SoC_{th} is emulated to be smaller than the battery SoC in this case ($SoC > SoC_{th}$). Initially, the PV is supplying power according to the load demand of 650 W and the battery is also not operating as the load demand is below $p_{pv\text{-}max}$ (800 W) and the SoC is larger than SoC_{th}. At $t = 0.5$ s, p_{load} suddenly increases from 650 W to 1000 W as illustrated in Fig. 6(b). Since p_{load} is larger than $p_{pv\text{-}max}$, the operation status Op is updated to 1, shown in Fig. 6(b). Hence, the PV increases its output power to the maximum available power and the battery converter is also in operation to supply the

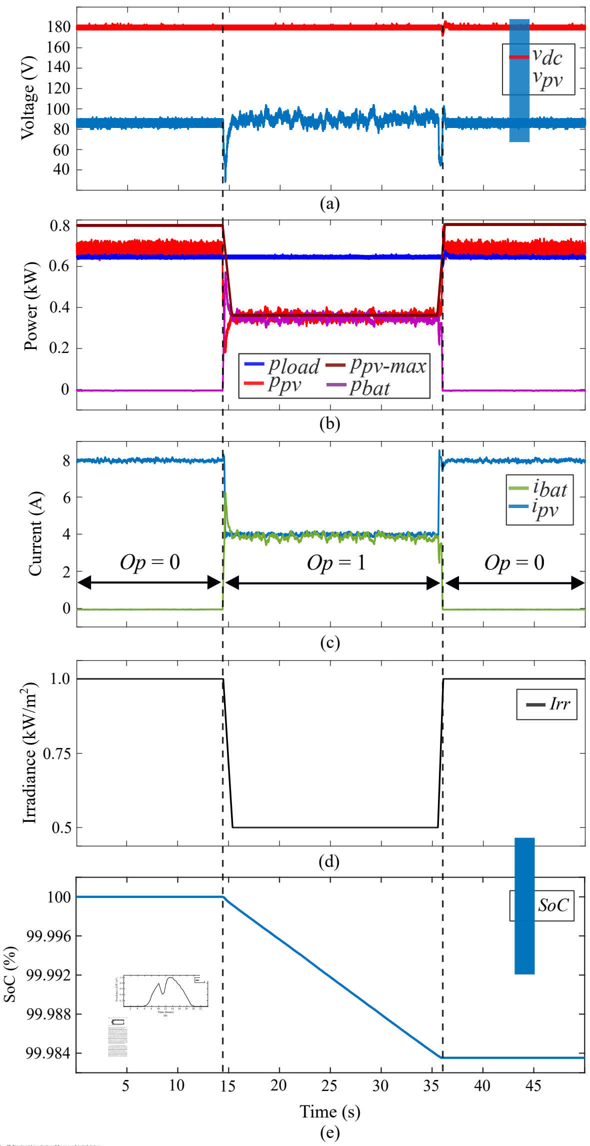

Fig. 8. *Case III*: Experimental investigation of the proposed control strategy under intermittent irradiance changes. (a) PV voltage, and dc-link voltage, (b) PV power, PV maximum power, load power and battery power, (c) PV and battery currents, (d) irradiance and (e) SoC.

($SoC > SoC_{th}$) and the load demand is fixed at 650 W. Initially, the PV is generating the load demand and the battery system is not in action. An increase in SoC_{th}, which is higher than the battery SoC ($SoC < SoC_{th}$), is emulated at $t = 0.5$ s. Subsequently, the operation mode Op is updated to -1 based on the proposed strategy in Fig. 3, as depicted in Fig. 7(b). Thus, the output of the PV is increased to the maximum possible value and any surplus generation from the PV system is supplied to the battery in order to increase the SoC, as demonstrated in Figs. 7(c) and (d). At $t = 1.5$ s, the battery SoC reaches its maximum limit SoC_{max} (95 % in this case). As a result, Op is updated to 0 and $p_{pv\text{-}ref}$ is set to the load demand plus the power deviation from the dc-link voltage regulation, described in (2). The BESS is also disconnected from the system and its current becomes zero, as shown in Fig. 7(d). In this case, it can be observed that the proposed

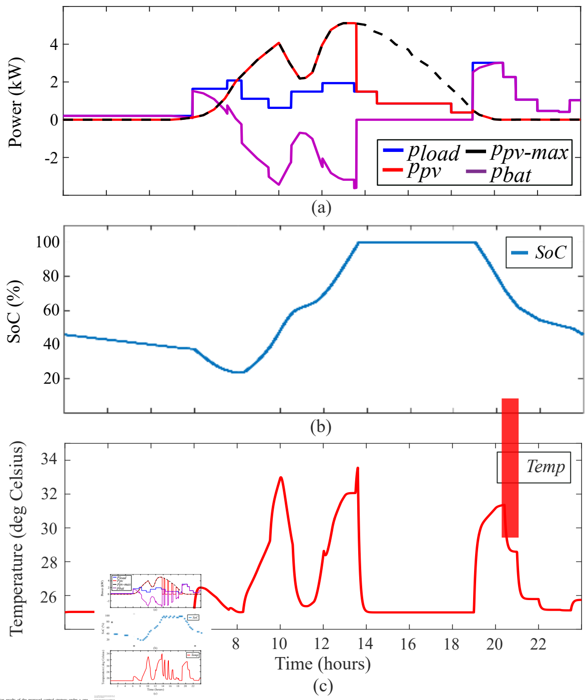

Fig. 11. Simulation results of the proposed control strategy under a one-day case study. (a) Load power, PV power, PV maximum power and battery power, (b) SoC, and (c) temperature.

of the selected Lithium-ion (Li-ion) battery ($3.3\,\mathrm{V}, 70\,\mathrm{Ah}$) are provided in [22]. The battery capacity is designed in such a way that the battery is effectively utilized (SoC variation between $100\,\%$ max. and $20\,\%$ min.). Accordingly, there are four parallel strings of 16 battery banks connected in series. Each battery bank has $70\,\mathrm{m}\Omega$ internal series resistance [23]. This resistance value is used to calculate the internal power losses of the battery. An electrcial equivalent circuit thermal model is implemented to analyze the battery cell temperature as shown in Fig. 10. T_{amb} is the ambient temperature and it is assumed to be $25\,^{\circ}\mathrm{C}$.

The power dissipation Q can be calculated as follows:

$$Q = \frac{T_{in} - T_{amb}}{R}, \tag{6}$$

where R is the heat transfer thermal resistance. The internal generated heat of the battery core is transferred via convection to the battery body and via conduction to the battery casing material. As shown in Fig. 10, there are two convective thermal resistance, R_{core} and R_{bat}, and one conductive thermal resistance R_{case}. Hence, total thermal resistance R is $R_{core} + R_{bat} + R_{case}$. With the Li-ion battery parameters (i.e. length, width, height dimensions of battery casing and body) from [22], R is calculated to be $6.4025\ \mathrm{K/W}$ based on (11) and (12) in the Appendix. The internal temperature of the Li-ion battery can be computed using (6) with the known internal power losses and thermal resistance values.

Apart from the temperature, other factors including the SoC, depth-of-discharge (DoD), cycle counts and the calendar aging also heavily influence the Li-ion battery lifetime. Therefore, the Li-ion battery aging model [24], which takes into account

Hence, the temperature of the battery decreases back to the room temperature. The battery only operates again when the PV power is insufficient for the load demand or the SoC drops below SoC_{th}. This Li-ion battery can be operated for 2552 days (assuming the same daily load and irradiance profiles), based on the model in (7), with the proposed control strategy before the battery reaches its end-of-life (EoL), which is assumed to be when the battery capacity drops below $80\,\%$ of its rated value.

In the conventional control strategy, the PV operates with the MPPT and the BESS operates continuously to effectively regulate the dc-link voltage v_{dc} by intaking all the power fluctuations from the load and the PV output [11], [16], [21]. When the battery SoC reaches to $SoC_{max} = 100\,\%$, the PV system is disconnected from the dcMG to prevent any overcharging issue since the MPPT is incapable of power adjustment (Fig. 12(a)), and only the battery is in operation. As a result of the battery supplying the load, the SoC of the battery decreases, as illustrated in Fig. 12(b). When the SoC reaches to $SoC_{th} = 95\,\%$, the PV operates again to charge the battery as shown in Fig. 12(b). The temperature fluctuations of the battery with the conventional control are relatively high since the internal power dissipation is large due to the continuous operation, as demonstrated in Fig. 12(c). According to the model in (7), the Li-ion battery can function for 1964 days before its capacity reaches to the EoL with the conventional control strategy.

In the following, the lifetime study is repeated for another common battery type, i.e. lead-acid (LA) battery. The battery lifetime is estimated based on the same load demand, PV generation, and battery utilization manners of the proposed and the conventional controls, as presented in Figs. 11 and 12. The rating of each LA cell is $2\,\mathrm{V}, 4\,\mathrm{Ah}$ and there are ten parallel strings of 30 battery banks connected in series. The overall heat transfer coefficient is $5.7\,\mathrm{WK^{-1}m^{-2}}$ for the thermal resistance from the cell to the surroundings. The thermodynamic properties of this battery are provided in [26]. Subsequently, the temperature/current dependence characteristic (9), which is experimentally analyzed in [26], is used to estimate the LA battery cell temperature.

$$T = 36.2I + 25 \tag{9}$$

Among the different LA battery degradation parameters, temperature is known to be the most impactful parameter. Hence, the remaining lifetime of the LA battery L_{LA} is estimated based on the accumulated thermal stress [27] as follows:

$$L_{LA}(t_x) = \frac{L_n - \sum_{i=1}^{x}(t_i - t_{i-1}) \times 2^{(T_i - 25)/\alpha}}{2^{(T_x - T_n)/\alpha}}, \tag{10}$$

where L_n is the nominal life of the LA battery, $(t_i - t_{i-1})$ is the time difference, T_i is the average temperature during the time period t_i, T_x is the temperature at time period t_x, and α=10 is the change in temperature coefficient.

Accordingly, the LA battery can last for 1112 days with the proposed control strategy and 778 days with the conventional control strategy before reaching the EoL. It is also noted that the lifetime of the LA battery is relatively shorter than the Li-ion battery [28].

Thus, this case study exhibits that the proposed control strategy prolongs the Li-ion battery aging, based on different battery degrading parameters, by $29.93\,\%$ as compared to the conventional control strategy (from 1964 days in the conventional control to 2552 days in the proposed control). Similarly, the gained lifetime of the LA battery with the proposed control strategy is around $42.93\,\%$ (from 778 days in the conventional control to 1112 days in the proposed control). Hence, the proposed control strategy demonstrates the significance of having FPPT capability for the PV systems in stand-alone dcMGs.

V. Conclusion

An enhanced control strategy for islanded dcMG with PV and BESS has been introduced in this paper. The proposed control strategy minimizes the utilization of the BESS by changing the control operation mode according to the dc-link voltage range and load power demand. It also upholds the SoC of the battery within the desired range if possible. The effectiveness and reliability of the proposed control strategy has been demonstrated with experimental results and a simulation case study. The results show that the proposed strategy is able to keep the dc-link voltage close to the desired reference even during transients on load or solar irradiance. The simulation case study shows how the FPPT based control eliminates partial cycles and reduces the battery temperature fluctuations and thus, extends the Li-ion battery lifetime by $29.93\,\%$ and the LA battery lifetime by $42.93\,\%$ compared to a conventional MPPT based control.

Appendix: Li-ion Battery Degradation Model

Thermal resistance of the battery core R_{core} and the battery body R_{bat} were obtained using the convective heat transfer equation, as given in (11). The battery casing thermal resistance R_{case} was obtained using the conductive heat transfer equation as follows:

$$R_{conv} = 1/(h \times Area) \tag{11}$$

$$R_{cond} = length/(k \times Area), \tag{12}$$

where h is the heat transfer coefficient and k is the casing thermal conductivity.

Subsequently, the four Li-ion battery degradation models that comprise the degradation rate f_d in (8) is as follows [24].

(i) Temperature stress model S_T: Battery operating temperature adversely affects the lifetime and the temperature effect in f_d is considered by S_T given in (13).

$$S_T = e^{0.0693(T-25)\times 25/T}, \tag{13}$$

where T is the internal battery working temperature, which can be obtained using (6).

(ii) SoC stress model S_σ: The effect of SoC on battery aging is considered by the following equation:

$$S_\sigma = e^{1.04(\sigma - 0.5)}, \tag{14}$$

where σ is the battery SoC at k^{th} sampling rate, which is estimated using (1). This model predicts higher denigration rate at higher SoC level, which is in line with expectations [29].

(iii) DoD stress model S_δ: DoD is a critically influential parameter for determining the battery degradation after a cycle. A larger DoD will result higher degradation rate as predicted by the following mode, which is specifically proposed for the selected Li-ion battery type [24].

$$S_\delta = (1.4\text{E}5 \times \delta^{-0.501} - 1.23\text{E}5)^{-1}, \tag{15}$$

where δ represents the battery DoD.

(iv) Time stress model S_t: This model is a linear function of time as follows:

$$S_t = t \times 4.14\text{E} - 10, \tag{16}$$

where t is the battery operation duration. The implemented Li-ion lifetime model in (7) not only considers the number of battery operation cycles, but also the battery working temperature, the cycle amplitudes (SoC and DoD models), as well as the battery calendar aging (when it is in standby mode) to achieve a realistic estimation in the battery lifetime.

REFERENCES

[1] International Energy Agency, "Renewable electricity generation by source," 2021. [Online]. Available: https://www.iea.org/data-and-statistics/charts?energy=solar.

[2] U. Manandhar, A. Ukil, and T. K. K. Jonathan, "Efficiency comparison of DC and AC microgrid," in *IEEE Innov. Smart Grid Tech. - Asia (ISGT ASIA)*, pp. 1–6, Nov. 2015.

[3] J. J. Justo, F. Mwasilu, J. Lee, and J.-W. Jung, "AC-microgrids versus DC-microgrids with distributed energy resources: a review," *Renewable and Sustainable Energy Reviews*, vol. 24, pp. 387 – 405, 2013.

[4] E. Dallago, A. Liberale, D. Miotti, and G. Venchi, "Direct MPPT algorithm for PV sources with only voltage measurements," *IEEE Trans. Power Electron.*, vol. 30, pp. 6742–6750, Dec. 2015.

[5] H. Elfeqy, M. Shahin, A. Al-Rumaihi, A. Massoud, and A. Gastli, "A highly efficient PV power system for DC microgrids," in *Proc. of IEEE Symposium on Computer Appl. Ind. Electron. (ISCAIE)*, pp. 183–188, May 2016.

[6] H. D. Tafti, G. Konstantinou, C. D. Townsend, G. G. Farivar, A. Sangwongwanich, Y. Yang, J. Pou, and F. Blaabjerg, "Extended functionalities of photovoltaic systems with flexible power point tracking: Recent advances," *IEEE Trans. Power Electron.*, pp. 9342–9356, Sep. 2020.

[7] H. D. Tafti, C. D. Townsend, G. Konstantinou, and J. Pou, "A multi-mode flexible power point tracking algorithm for photovoltaic power plants," *IEEE Trans. Power Electron.*, vol. 34, pp. 5038–5042, Jun. 2019.

[8] H. D. Tafti, A. Sangwongwanich, Y. Yang, J. Pou, G. Konstantinou, and F. Blaabjerg, "An adaptive control scheme for flexible power point tracking in photovoltaic systems," *IEEE Trans. Power Electron.*, vol. 34, pp. 5451–5463, Jun. 2019.

[9] A. Sangwongwanich, Y. Yang, and F. Blaabjerg, "A sensorless power reserve control strategy for two-stage grid-connected PV systems," *IEEE Trans. Power Electron.*, vol. 32, pp. 8559–8569, Nov. 2017.

[10] S. Sahoo, S. Mishra, S. Jha, and B. Singh, "A cooperative adaptive droop based energy management and optimal voltage regulation scheme for DC microgrids," *IEEE Trans. Ind. Electron.*, vol. 67, pp. 2894–2904, Apr. 2020.

[11] G. C. Konstantopoulos and A. T. Alexandridis, "Non-linear voltage regulator design for DC/DC boost converters used in photovoltaic applications: analysis and experimental results," *IET Renew. Power Gen.*, vol. 7, pp. 296–308, May 2013.

[12] A. Tofighi and M. Kalantar, "Power management of PV/battery hybrid power source via passivity-based control," *Renewable Energy*, vol. 36, pp. 2440 – 2450, Sep. 2011.

[13] H. Cai, J. Xiang, W. Wei, and M. Z. Q. Chen, "V-dp/dv droop control for PV sources in DC microgrids," *IEEE Trans. Power Electron.*, vol. 33, pp. 7708–7720, Sep. 2018.

[14] P. Ruetschi, "Aging mechanisms and service life of lead-acid batteries," *Power Sources*, vol. 127, pp. 33–44, Mar. 2004.

[15] B. Shabani and M. Biju, "Theoretical modelling methods for thermal management of batteries," *Energies*, vol. 8, pp. 10153–10177, Sep. 2015.

[16] H. Mahmood, D. Michaelson, and J. Jiang, "Decentralized power management of a PV/battery hybrid unit in a droop-controlled islanded microgrid," *IEEE Trans. Power Electron.*, vol. 30, pp. 7215–7229, Dec. 2015.

[17] Y. Shan, J. Hu, K. W. Chan, Q. Fu, and J. M. Guerrero, "Model predictive control of bidirectional DC/DC converters and AC/DC interlinking converters - a new control method for PV-Wind-Battery microgrids," *IEEE Trans. Sustain. Energy*, vol. 10, pp. 1823–1833, Oct. 2019.

[18] T. Dragicevic, J. M. Guerrero, J. C. Vasquez, and D. Skrlec, "Supervisory control of an adaptive-droop regulated DC microgrid with battery management capability," *IEEE Trans. Power Electron.*, vol. 29, pp. 695–706, Feb. 2014.

[19] G. Angenendt, S. Zurmuhlen, H. Axelsen, and D. U. Sauer, "Comparison of different operation strategies for PV battery home storage systems including forecast-based operation strategies," *Appl. Energy*, vol. 229, pp. 884–899, Nov. 2018.

[20] A. Narang, H. D. Tafti, C. D. Townsend, G. Farivar, J. Pou, G. Konstantinou, and S. Vazquez, "An algorithm for fast flexible power point tracking in photovoltaic power plants," in *Proc. of IECON*, vol. 1, pp. 4387–4392, Oct. 2019.

[21] Y. Yang, Y. Qin, S. Tan, and S. Y. R. Hui, "Efficient improvement of photovoltaic-battery systems in standalone DC microgrids using a local hierarchical control for the battery system," *IEEE Trans. Power Electron.*, vol. 34, pp. 10796–10807, Nov. 2019.

[22] Y. Xiao, "Model-based virtual thermal sensors for lithium-ion battery in EV applications," *IEEE Trans. Ind. Electron.*, vol. 62, pp. 3112–3122, May 2015.

[23] EEMB, "Li-ion battery datasheet," 2021. [Online]. Available: https://www.ineltro.ch/media/downloads/SAAItem/45/45958/36e3e7f3-2049-4adb-a2a7-79c654d92915.pdf.

[24] B. Xu, A. Oudalov, A. Ulbig, G. Andersson, and D. S. Kirschen, "Modeling of Lithium-Ion battery degradation for cell life assessment," *IEEE Trans. Smart Grid*, vol. 9, pp. 1131–1140, Mar. 2018.

[25] M. Musallam and C. M. Johnson, "An efficient implementation of the rainflow counting algorithm for life consumption estimation," *IEEE Trans. Reliability*, vol. 61, pp. 978–986, Dec. 2012.

[26] D. Valkovska, M. Dimitrov, T. Todorov, and D. Pavlov, "Thermal behavior of VRLA battery during closed oxygen cycle operation," *J. Power Sources*, vol. 191, pp. 119–126, Oct. 2009.

[27] P. E. Pascoe and A. H. Anbuky, "Standby power system VRLA battery reserve life estimation scheme," *IEEE Trans. Energy Convers.*, vol. 20, pp. 887–895, Dec. 2005.

[28] S. Dhundhara, Y. P. Verma, and A. Williams, "Techno-economic analysis of the lithium-ion and lead-acid battery in microgrid systems," *Energy Convers. and Manage.*, vol. 177, pp. 122–142, Dec. 2018.

[29] K. Laidler, "The development of the Arrhenius equation," *J. of Chem. Educ.*, vol. 61, pp. 494–498, Jun. 1984.